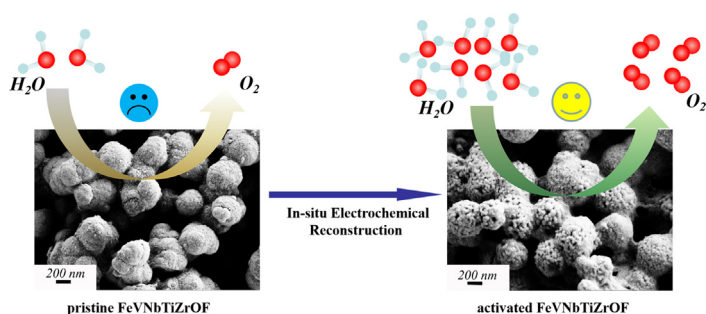Regular Article

In-situ reconstruction of non-noble multi-metal core-shell oxyfluorides for water oxidation

Yin'an Zhu [1], Weiji Dai [1], Xu Zhong, Tao Lu, Ye Pan *

School of Materials Science and Engineering, Jiangsu Key Laboratory of Advanced Metallic Materials, Southeast University, Nanjing 211189, China

GRAPHICAL ABSTRACT

ARTICLE INFO

ABSTRACT

The electrochemical anodic behavior of transition metal compounds plays an undeniably non-negligible role across many electrooxidation reactions. In this work, a chronopotentiometric technique was employed to activate the multicomponent non-noble metal oxyfluorides in-situ for oxygen evolution reaction (OER). It is interesting to unravel that the increasing applied current density helps to reconstruct the catalyst into nanoporous core–shell structure and introduce metal oxyhydroxide on the surface, which guarantees more channels for efficient ion/mass transportation and thus contributes to exposing more active sites for catalytic reaction. The activated five-membered oxyfluoride shows the best catalytic activity with overpotential of 348 ± 2 mV to achieve the current density of 10 mA/cm^2 and a Tafel slope of 110.3 ± 0.1 mV/dec, in contrast with the pristine one (532 ± 2 mV & 240.2 ± 0.1 mV/dec). It still maintains high stability after long time OER measurement, making it a promising succedaneum for noble metal catalysts. The high-entropy effect, amorphous state and high active sites density jointly contribute to its enhanced OER performance. This work provides new ideas for realizing the potential of inactive elements via entropy engineering and using electrochemical self-reconstruction to modify semiconductors for advanced water oxidation.

© 2021 Elsevier Inc. All rights reserved.

1. Introduction

Water electrolysis is widely regarded as a promising means of producing high purity oxygen and hydrogen gas due to sufficient water supplements and zero carbon emission [1]. OER and hydrogen evolution reaction (HER) constitute the entire water electrolysis, both necessitating electrocatalysts to lower corresponding overpotentials. Despite perfect performance provided by platinum group catalysts for HER, the another half (OER) is a bottleneck reaction due to the unfavorable kinetics involving the 4-electron proton transfer process, making it the rate-determining step with

---

* Corresponding author.
  E-mail address: panye@seu.edu.cn (Y. Pan).
[1] Yin'an Zhu and Weiji Dai contributed equally to this work.

higher overpotentials [2]. The overall efficiency of water electrolysis is considerably impeded. Though ruthenium and iridium catalysts can accelerate oxygen evolution efficiency to some extent, the overpotentials and kinetics parameters are far from satisfactory. Besides, the high cost and scarce storage still challenge the commercial noble metal catalysts for large-scale applications in water splitting [3]. Thus, developing inexpensive and high-efficient electrocatalysts to catalyze HER/OER is extremely urged on the agenda.

So far, a series of researchers have found that most OER catalysts, including sulfides, borides, phosphides, nitrides, carbides, alloys, and oxides, are the precatalysts actually [4–10]. Once immersed into electrolytes and activated, these materials will undergo an irreversible and sharp structural evolution into metal oxides/oxyhydroxides on the surface during OER. When referred to the alkaline milieu and elevated applied potentials, differences in morphologic structure are more pronounced before and after measurements [11]. Indeed, the aggregation of the oxidation outer layers and the pristine compounds is deemed the actual electrocatalysts, rather than the as-prepared one. The electrocatalytic reactions are universally acknowledged to take place at the electrode/electrolyte interface. As a result, the activated species on the surface of the materials play a critical role in OER process. Wang et al. reported a facile in-situ electrochemical conversion technique for initiating γ-NiOOH amorphous shell around the initial catalysts, which significantly improves the OER activity [12]. With the increasing applied potentials, the outer shell underwent a transition from NiNPS to α-Ni$(OH)_2$ / NiO, to γ-NiOOH. Our group recently has found that surface reconstruction of phosphide precatalyst ingeniously leads to in-situ P doping into NiO lattice. In contrast to bare NiO, the induction of P activates the Ni sites in NiO to a great extent and weakens the bonding strength of the intermediates [13]. Following such an idea, in-situ electrochemical surface reconstruction is a potential means to grow active components on the relatively inactive substrate for advanced OER performance.

Metal oxyfluorides are conventionally used to work as Li-ion cathodes, supercapacitors, and photocatalysts owing to the excellent electrochemical/chemical properties [14–16]. Recently, their applications in electrocatalysis, especially water oxidation, have been gradually reported [17,18]. Lhoste's group employed a microwave-assisted solvothermal method to synthesize NiFe-O-F with excellent activity and stability [19,20]. Meanwhile, Wang and his co-authors synthesized a fluoride-incorporating NiFe hydroxide nanosheet array. The following cyclic voltammetry cycling dramatically increased the electrocatalytic activity [21]. Most of these works focused on NiFe-based fluorinated materials for two reasons. On the one side, the electronegativity of fluorine anion is the highest, enabling it easier to dissolute into alkaline electrolyte under oxidation potential [22,23]. It means the existence of Metal-F bond in oxyfluorides would be more conducive to catalyzing the formation of metal oxyhydroxides during anodic activation, in contrast with Metal-P/S/N/Se bonds. On the other side, activated products derived from NiFe species generally show higher catalytic performance for efficient and durable water electrolysis [24]. Nevertheless, OER research associate with other metal oxyfluorides are scant. Herein, we synthesized a multicomponent non-noble metal oxyfluoride by a facile dealloying approach basing on ZrNi-based amorphous alloys. A series of current densities were applied to in-situ construct nanoporous and catalytically active oxyhydroxides on the surface of metal oxyfluorides. Compared with the pristine sample, the activated catalyst possesses lower overpotential and improved reaction kinetics in OER. Most importantly, metal elements in as-prepared oxyfluoride are relatively inexpensive and inactive, including V, Ti, and Nb. Modifying Fe with these elements through entropy engineering finally facilitates an active and stable OER catalyst.

2. Experiment section

2.1. Materials

High-purity (>99.95%) metal of Zr, Ni, Fe, Ti, V, and Nb were brought from Beijing China New Metal Co., Ltd. KOH, RuO_2, HF (wt 40%) and H_2O_2 (wt 30%) were all purchased from Aladdin Chemistry Co. Ltd.

2.2. Preparation of dealloying precursors

Amorphous alloy of $Zr_{60}Ni_{20}Fe_5V_5Ti_5Nb_5$ was synthesized via a melt spinning method in high pure Ar atmosphere. The obtained ribbons were cut into fragments with 2 mm in width and 3 cm in length for sufficient reaction. In addition, ribbons composed of $Zr_{60}Ni_{20}Fe_{6.67}Ti_{6.66}Nb_{6.66}$, $Zr_{60}Ni_{20}Fe_{10}Nb_{10}$ and $Zr_{60}Ni_{20}Fe_{20}$ were also prepared for comparison.

2.3. Preparation of core–shell structures

The dealloying process was performed under 55℃ within 24 h. A mixture of HF (0.1 mol L^{-1}) and H_2O_2 was served as the corrosive media. After dealloying, yellow precipitates (pristine FeVNbTiZrOF) were collected and washed with deionized water, then dried at drying oven at room temperature for 3 h.

2.4. Preparation of working electrodes

For the synthesis of our working electrodes, 50 mg of dealloying powders and 50 μL Nafion were dispersed into 3950 μL ethanol. Then the mixture was put in ultrasonic bath for 60 min to obtain a uniform catalyst ink. Subsequently, several well-tailored (5*30 mm) rectangle carbon fiber papers were ultrasonically cleaned in hydrochloric acid and ethanol for 20 min and dried in air. Next, the carbon fiber paper was laid flat in the as-prepared uniform catalyst ink for 20 min to load catalyst naturally through gravity. At last, the carbon fiber paper loaded with the non-noble multicomponent metal oxyfluoride powders (0.8 mg/cm^2, 1 cm^2) was taken out and dried at 60℃ to eliminate the interference of ethanol for subsequent tests.

2.5. In-situ surface reconstruction of core–shell structures

Surface activation and reconstruction of the core–shell structures were conducted by a chronopotentiometric technique using an electrochemical workstation (CHI 660E) with different constant current densities at 5, 10, 20, and 40 mA/cm^2 for 20 h in 1 M KOH. The corresponding products were thereby named as FeVNbTiZrOF-CC-5, FeVNbTiZrOF-CC-10, FeVNbTiZrOF-CC-20, and FeVNbTiZrOF-CC-40, respectively.

2.6. Electrochemical measurements

All the electrochemical measurements in our work were conducted with a standard three-electrode system. 1 M KOH was used as electrolyte. A saturated calomel electrode and graphite rod were used as the reference electrode and counter electrode, respectively. The dealloying products loaded on carbon fiber paper works as the working electrode. Besides, all the potentials were referenced to a reversible hydrogen electrode (RHE) using the equation of E_{RHE} = $E_{Hg/HgO}$ + 0.059 pH + 0.24. The overpotential (η) was calculated according to the following formula: η = E_{RHE} − 1.23 V. The electrochemical activities of the catalysts were measured at a scan rate of 5 mV/s by Linear Scanning Voltammetry (LSV). To record the electrochemical active surface area of the catalysts, cyclic voltammo-

gram curves (1.155–1.255 V vs RHE) were performed with the scan rates of 10, 20, 30, 40, 50 and 60 mV/s. The double layer capacitance (C_{dl}) of testes samples were then obtained from plotting $\Delta J = (J_a - J_c)_{@1.205\ V\ vs\ RHE}$ against the scan rates. The linear slope is equivalent to twice of C_{dl}, which can be employed to represent the electrochemical active surface area. Durability test of the best-performance catalyst was carried out at a constant overpotential for 48 h. All the electrochemical impedance spectroscopy spectra (EIS) were measured at the same potential (1.47 V vs RHE) with frequency range from 100 kHz to 0.01 Hz. In particular, to assess the intrinsic activity of the catalysts, the normalized LSV curves were compensated with 90% IR.

2.7. Characterization

The crystallinity of powders was confirmed by the D8 Bruker X-ray diffraction with Cu Kα radiation. UV–vis spectrophotometer (UV-2600) was used to investigate the light absorption of catalysts. Zeiss and FEI field emission scanning electron microscope was used to investigate the surface morphology of powders. HAADF-STEM images and element mappings before and after chronopotentiometric treatment were characterized via transmission electron microscopy (FEI G2-F30 and Talos F200X). The chemical valence and composition were analyzed by a Thermo ESCALAB 250XI.

3. Results and discussions

The preparation of the oxyfluorides undergoes a dealloying method basing on $Zr_{60}Ni_{20}Fe_5V_5Ti_5Nb_5$ amorphous ribbons (Fig. S1, Table S1), illustrating in Fig. 1. Traditional dealloying method has been applied to synthesize nanoporous skeletons by selective removal of non-precious metal [25,26]. It was recently found the dealloying products change with the variation of the corrosive media. For instance, a mixture of acidic and oxidative remedies ($H_2C_2O_4$ / H_2O_2) could directly corrode the amorphous alloy into insoluble oxalate precipitation [27]. Inspired by this idea, we employed HF/H_2O_2 as the corrosive medium with reactions below. Firstly, Ni and partial Zr of ribbons dissolve into the oxidative and acidic solution in the form of Ni^{2+} and ZrF_6^{2-}, respectively. Original amorphous state of the ribbon cannot sustain any more. The surface etching pits allow HF / H_2O_2 to react with Fe/V/Nb/Ti and rest Zr to from corresponding oxyfluorides (Fig. S2). Due to large surface area and high energy, the small and solo nanospheres irreversibly accumulated into larger Siamese particles and detached from the ribbon substrate.

XRD pattern of the dealloying product is shown in Fig. 2a. The full width at half maximum of two halo peaks for the pristine FeVNbTiZrOF are apparently wide, indicating it an amorphous phase with long-range disorder and short-range order. DRS spectrum (Fig. S3) proves the pristine FeVNbTiZrOF is a semiconductor with wide band gap of 2.99 eV. SEM image in Fig. 2b displays the yellow dealloyed powders, consisting of solo or conjoined nanospheres with an average diameter of approximately 500 nm. Interestingly, a detailed insight (Fig. 2c) into the broken sphere reveals the pristine FeVNbTiZrOF features obviously a core–shell structure, which is mainly composed of agglomerated smaller nanoparticles. TEM images (Fig. 2d) further give the thickness of outer shell (~35 nm). Besides, in Fig. 2f and g, both line scan and EDS mapping demonstrates the component inhomogeneity between the shell and core. Zr enriches in the former whereas Fe/V/Nb/Ti accumulates in the latter. The compositional ununiformity in pristine FeVNbTiZrOF may implies a spinodal decomposition during its formation process, of which Fe/V/Nb/Ti and Zr oxyfluorides are immiscible with each other, thereby establishing the core–shell structure. The widely accepted criterion for judging the multi-

component system is the mixing entropy (ΔS_{mix}). If ΔS_{mix} exceeds a certain value, the system is of high entropy. To simplify the calculation, the core of the as-prepared multi-component oxyfluorides are calculated to be $FeVNbTiO_6F_5$ according to the EDS data (Table S1). Then ΔS_{mix} can be calculated by the formula $\left(\Delta S_{mix} = -R\left[\left(\sum_{i=1}^{N} x_i \ln x_i\right)_{cation-site} + \left(\sum_{j=1}^{M} x_j \ln x_j\right)_{anion-site}\right]\right.$, where R represents the ideal gas constant, x_i and x_j are the mole fractions of the metal elements and nonmetal elements, respectively.) and the value is 1.455 R, which outperforms the medium-entropy alloy (1.1 R) [28]. Thus, the pristine FeVNbTiZrOF is composed of high-entropy oxyfluoride core and Zr oxyfluoride shell.

Prior to OER testing, we employed chronopotentiometric technique to monitor what the anodic activation impacts on metal oxyfluorides, particularly in electrocatalytic activities. For the incremental component oxyfluorides activated at 5 mA/cm², we listed their overpotentials required to drive a current density of 20 mA/cm² (Fig. 3a). All activated oxyfluorides outperform the reference of RuO_2, suggesting them to be promising substitutes for noble metal OER catalysts. Besides, their overpotentials are gradually reduced with the addition of metal element in oxyfluorides, of which FeVNbTiZrOF-CC-5 takes the lowest overpotential (414 ± 2 mV). The performance of FeVNbTiZrOF-CC-5, however, is still high and far from satisfactory for industrial application. To deeply discuss what the oxidation environment is beneficial for improving OER activity, a series of constant current densities (5, 10, 20, and 40 mA/cm² for 20 h) were applied (Fig. S4). In contrast with the pristine FeVNbTiZrOF, a small applied current density (5 mA/cm²) can greatly improve its electrocatalytic performance. Furthermore, when reaching up to 40 mA/cm², the activated oxyfluoride (FeVNbTiZrOF-CC-40) presents the highest catalytic activity with overpotential of 348 ± 2 mV and 388 ± 3 mV to achieve current densities of 10 mA/cm² and 20 mA/cm², respectively, which is acceptable among many fluorinated materials (Table S2). It could be inferred that the applied current density indeed helps to enhance the OER activity of oxyfluoride semiconductor. High current density generally means the harsh oxidizing atmosphere, making it more easily to activate catalyst surface and produce active sites. Unfortunately, further increasing current density would destroy the structure of supporter and it is unable to measure the oxygen evolution process.

Tafel analysis offers intrinsic insights into the OER mechanism occurring on catalyst surface. The lowest Tafel slope implies the fastest response of electrocatalytic current with the increasing applied potential. The corresponding fitted Tafel plots of the activated oxyfluorides are displayed in Fig. 3c. The pristine FeVNbTiZrOF exhibits a much higher Tafel slop of 242.0 ± 0.1 mV dec⁻¹. It can be rapidly reduced once activated as follows: FeVNbTiZrOF-CC-5 (139.2 ± 0.1 mV dec⁻¹), FeVNbTiZrOF-CC-10 (133.2 ± 0.2 mV dec⁻¹), FeVNbTiZrOF-CC-20 (126.7 ± 0.2 mV dec⁻¹), FeVNbTiZrOF-CC-40 (110.3 ± 0.1 mV dec⁻¹). The electrocatalytic efficiency of active sites is quite critical in OER process. The number of active sites is roughly proportional to electrochemical active area (Fig. 3d) which can be tested by the C_{dl} derived from the cyclic voltammetry (Fig. S5). Therefore, the higher C_{dl} (10.15 ± 0.02 mF) evidences the larger electrochemical active area of FeVNbTiZrOF-CC-5, much higher than the pristine FeVNbTiZrOF (0.16 ± 0.002 mF). Simultaneously, this value is elevated with the increasing applied current density and reaches a maximum at 11.28 ± 0.04 mF for FeVNbTiZrOF-CC-40. It demonstrates again the electrochemical reconstruction is an effective method for engineering surface active sites. Electrocatalytic kinetics and interfacial properties of the catalysts are further investigated by EIS and Nyquist plots are fitted via an equivalent circuit model of (R(CR)W). This model consists of a solution resistance (R_s) in series with a parallel con-
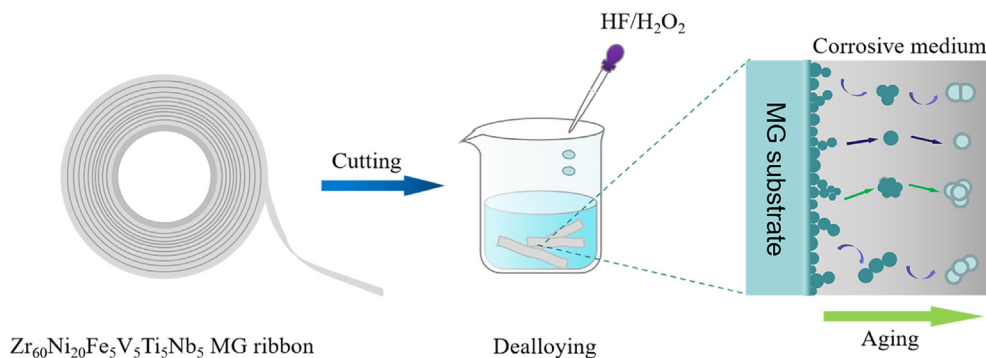
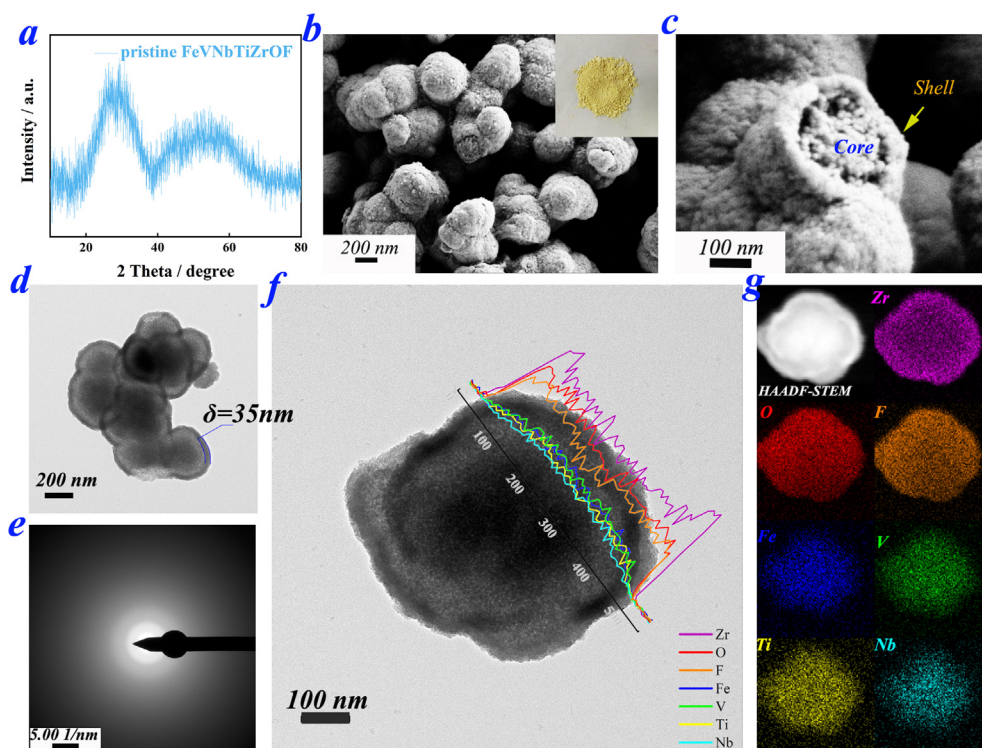**Fig. 1.** Schematic procedure to prepare the pristine FeVNbTiZrOF.

Fig. 2. (a) XRD pattern; (b, c) SEM images; (d–f) TEM images and (g) EDS mappings of the pristine FeVNbTiZrOF, the insert map is the optical photo of the pristine FeVNbTiZrOF.

nection of C_{dl} and charge transfer resistance (R_{ct}) and a Warburg impedance. An intuitive appreciation of Fig. 3e and Table S3 authenticates the effect of electrochemical reconstruction, impressively decreasing R_{ct} of pristine FeVNbTiZrOF from about 4966 ± 147 to 144.6 ± 2.2 Ω (FeVNbTiZrOF-CC-5). This value can be further lowered by intensifying the applied current density and it reaches minimum for FeVNbTiZrOF-CC-40 (105.7 ± 2.0 Ω). Meanwhile, the value of C_{dl} stemmed from the model also follows the same order as the result of ECSA. The lowest R_{ct} illustrates that FeVNbTiZrOF-CC-40 possesses a superior surface electron transfer ability as well as lower energy barrier for OER in comparison with the pristine one [29]. Lastly, a long-term electrocatalytic stability of FeVNbTiZrOF-CC-40 was also measured by chronoamperometry test with a constant applied potential at 1.578 V vs RHE (Fig. 3f). The monitored catalytic current density is quite stable with only a percentage of 4.61% loss after 48 h test. On the contrary, ruthenium dioxide, the benchmark commercial OER catalyst, shows deteriorating stability at the initial 2 h and then slowly returns.

The above-mentioned results indicates that FeVNbTiZrOF-CC-40 is a promising candidate for electrochemical water oxidation.

The superior OER activity of the FeVNbTiZrOF-CC-40 could be clarified according to the ex-situ composition and structure evolution through the activation. XRD pattern confirms FeVNbTiZrOF-CC-40 is still of amorphous structure (Fig. S6). Fig. S7 compares the elements of the pristine and activated FeVNbTiZrOF, including Zr, Fe, V, Nb, Ti, O and F. Due to the extremely low content of Fe/V/Nb/Ti elements in the shell, their characteristic signals are nowhere to be found. With respect to other elements, the peaks located at 184.6 and 187.0 eV may be assigned to $3d_{5/2}$ and $3d_{3/2}$ of Zr oxyfluorides, respectively [30]. After activation, it is rapidly oxidized into the highest valance state (IV), and therefore a shift of 1.2 eV is observed [31]. For O 1 s, signals before and after activation could be decomposed into different peaks (O_I, O_{II}, O_{III} and O_{IV}). Of them, O_I (530.9 eV) is related to the lattice oxygen [32]. O_{II}, O_{III} and O_{IV} belongs to the surface oxygen adsorption [33] oxyhydroxides [34] and the Nafion utilized in the electrocatalyst ink fabrication
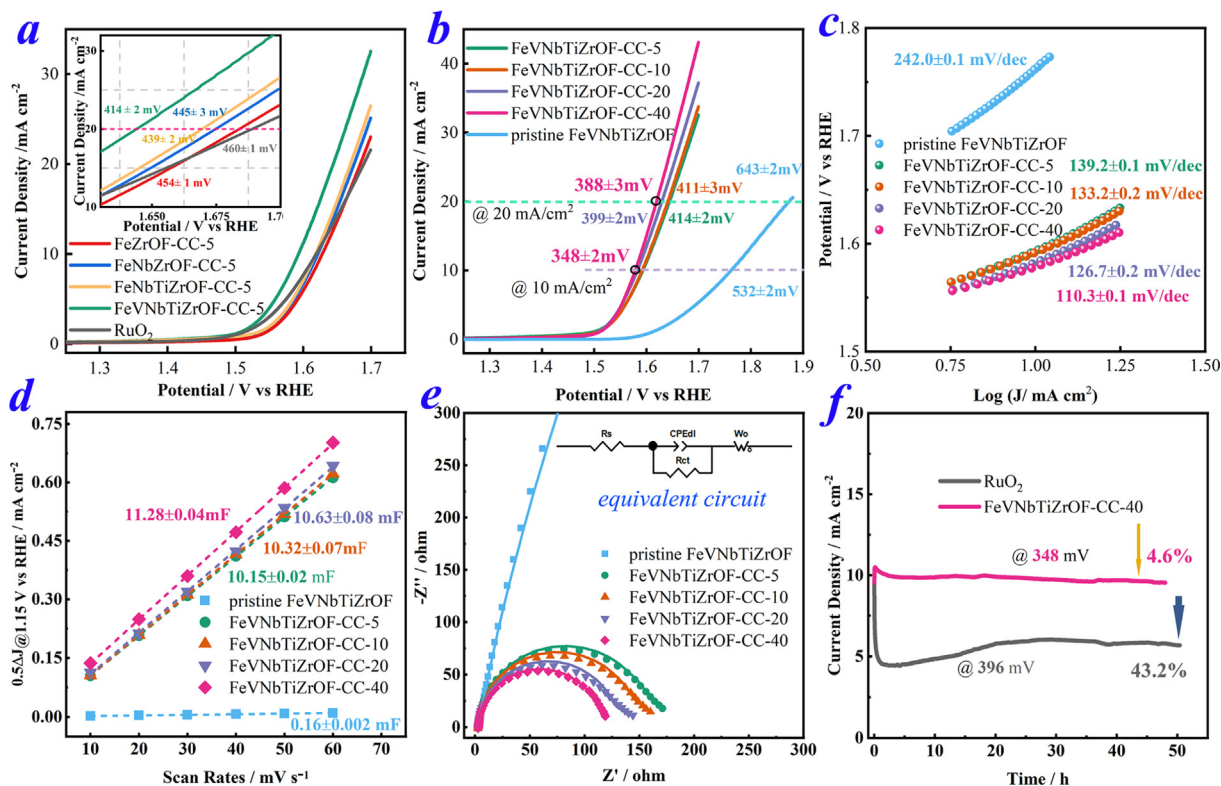
Fig. 3. Electrocatalytic activities of dealloying products and reference samples. All the LSV measurement was repeated for three times. (a) LSV curves of FeZrOF-CC-5, FeNbZrOF-CC-5, FeNbTiZrOF-CC-5, FeVNbTiZrOF-CC-5 and RuO$_2$ in 1 M KOH solution with a scan rate of 5 mV/s; (b) LSV curves of the pristine and activated FeVNbTiZrOF at different current densities; (c) corresponding Tafel plots; (d) corresponding linear plots of capacitive current densities vs scan rates; (e) Nyquist plots recorded at 1.47 V (vs. RHE). The corresponding equivalent circuit is depicted in the inset; (f) Chronoamperometric response of FeVNbTiZrOF-CC-40 and RuO$_2$ at the overpotential of 348 mV and 396 mV, respectively.

[35], respectively. For F 1s, the peaks at 689.7 eV and 685.2 eV are identified as the C-F bond (from Nafion) and the F-Zr bond, respectively. A more detailed contrast between the pristine and activated FeVNbTiZrOF exhibits opposing principles for O 1 s and F 1 s (Fig. 4). The electrochemical reconstruction dramatically destroys the Zr-F bond and synchronously increases the oxyhydroxide content. The higher current densities applied on pristine FeVNbTiZrOF are, the more obvious the main trend is. When increasing to 40 mA/cm^2, the content of oxyhydroxides reaches a maximum (85.08%) and Zr-F falls to minimum (1.06%). A credible explanation involves the impact of F anion, who has the strongest electronegativity to form an ionic M—F bond. This bond is easier oxidized and reconstructed into the surface metal oxyhydroxide than M—S/P/Se. Considering Zr species are harder to oxidize or reduce without extra power, we believe the successful establishment of Fe/V/Nb/Ti oxyhydroxide in the core of the activated FeVNbTiZrOF. The obtained metal oxyhydroxides are widely considered as active sites for efficient adsorption/desorption during OER process according to reaction mechanism [36,37].

SEM images of the activated FeVNbTiZrOF under diverse current densities are depicted in Fig. 5. Unlike the dramatic surface change (commonly from 3-D nanoparticles into 1-D or 2-D nanosheets) of borides or sulfides during electrochemical oxidation [38,39], the activated FeVNbTiZrOF displays unique surface variation. After activation at 5 mA/cm^2, several small irregular pores are formed at the junctions of the nanospheres. Due to the fact that pristine FeVNbTiZrOF itself is composed of accumulated particles, the intervals would be enlarged under the supply of external energy, as asserted by the Ostwald ripening mechanism [40]. Therefore, further raising current density leads to the higher coverage and larger size of nanopores. This expansion becomes more vivid after the

long-term catalytic stability test (Fig. S8). It is worth mentioning in insert map of Fig. 5d that the activated FeVNbTiZrOF finally reconstructs into nanoporous core–shell structure. The unique structure guarantees more channels for sufficient ion diffusion, mass transportation and exposing more active sites at the electrolyte/electrode interface. This scene was further confirmed by its TEM image, as depicted in Fig. 6, where the outer shells are partially interrupted by several nanopores. A closer insight into the high-resolution TEM image manifests the activation process not only creates nanoporous architecture, but also modifies the surface oxyfluoride into an amorphous zirconium oxyhydroxide layer with approximately 2 nm. Besides, the high content of oxygen in EDS data (Table S1 and Fig. S9) also proves the transformation from the oxyfluoride to oxyhydroxide. The obtained result is in a well agreement with that of XPS.

To reflect the intrinsic electrocatalytic activity, the polarization LSV curves of the pristine and activated FeVNbTiZrOF are normalized by ECSA so as to eliminate the amplification deriving from the increasing specific surface area and catalyst loading [41]. As shown in Fig. 7a, overpotential of the pristine FeVNbTiZrOF is reduced by 30 mV after activation when referring to 0.1 mA/cm^2. The improved intrinsic activity illustrates the formation of many active sites on catalysts surface, which is critical to optimizing the adsorption/desorption kinetic of OER intermediates. Apart from the compositional and structural explanations mentioned above, the experiment results also reveal the key impacts of the multi-component metal oxyfluoride itself, a combination of amorphous and high-entropy essence. For amorphous structure, the disorder atomic arrangement endows plentiful oxygen vacancies and metal vacancies, leading to bonds with random orientations, higher density of coordinatively unsaturated sites, and high surface energy
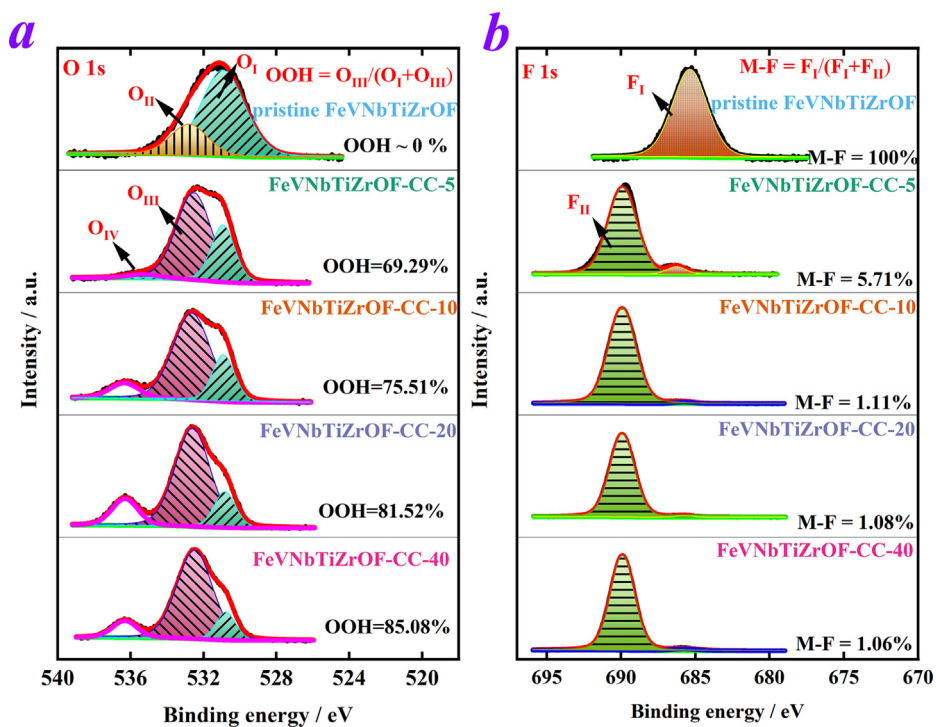
Fig. 4. XPS spectra of O 1s and F 1s of the pristine and activated FeVNbTiZrOF.
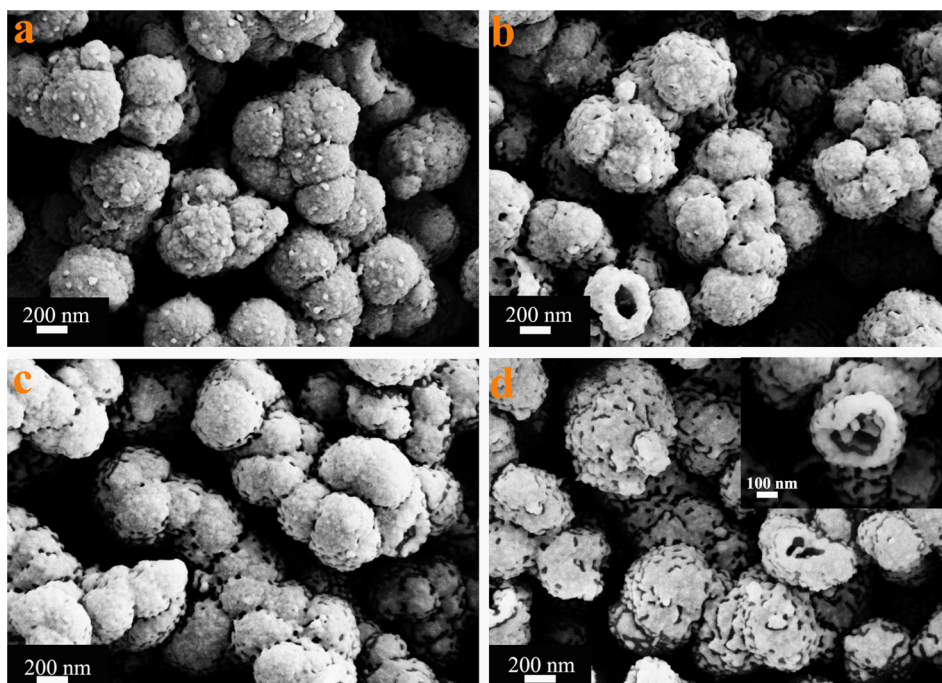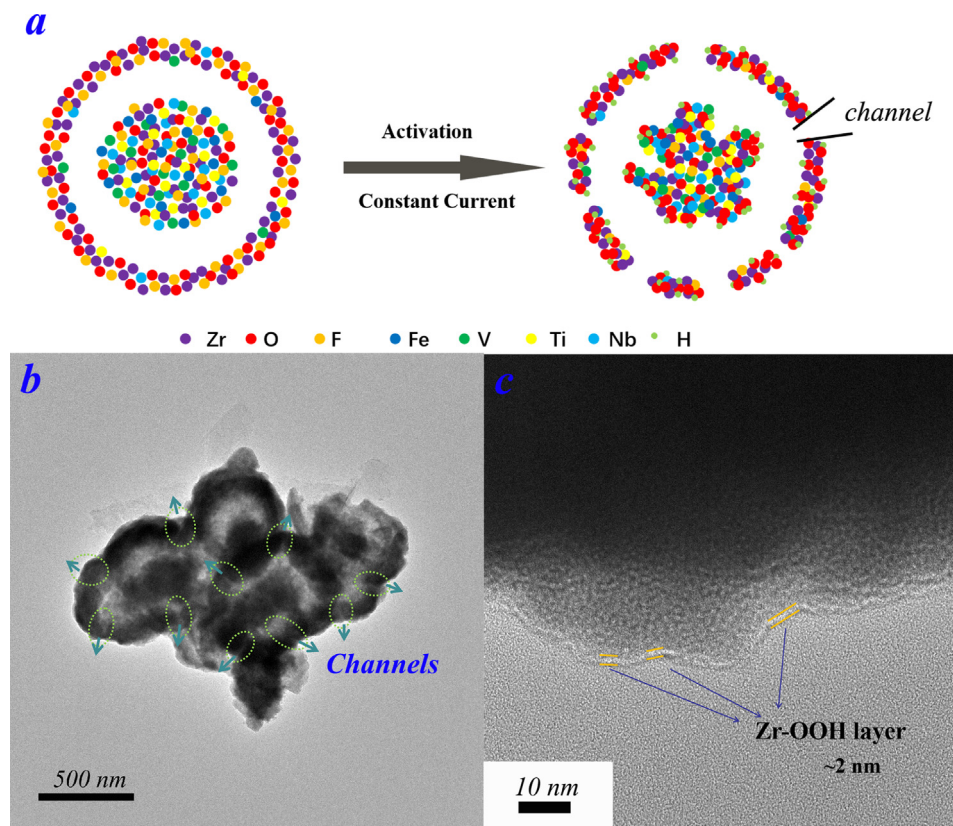

Fig. 5. SEM images of (a) FeVNbTiZrOF-CC-5; (b) FeVNbTiZrOF-CC-10; (c) FeVNbTiZrOF-CC-20; (d) FeVNbTiZrOF-CC-40.

[42,43]. These unique properties are conducive to reducing the adsorption energy of intermediates and energy barrier of catalytic reaction, thereby accelerating the charge transfers between the intermediates/active sites and raising the electrochemical catalytic performance [44,45]. For high-entropy materials, there exists strong mutual interactions among the multiple metal elements, which is unattainable in conventional single-metal ones [46,47]. When progressively introducing more metal elements into a sim-

ple compound, its chemical coordination environment and electronic structure are changed accordingly [48–50]. Besides, the surface neighboring active sites in high-entropy catalysts with different local electronic structures could provide the possibility for complementing the catalytic shortcomings of pure phases [51,52], for instance, weak electrical conductivity and molecule adsorption/desorption. This unexpected synergistic effect can significantly adjust the binding energy of oxygenated intermediates

Fig. 6. (a) Sketch map of electrochemical reconstruction (b) TEM image and (2) HRTEM image of the activated FeVNbTiZrOF.
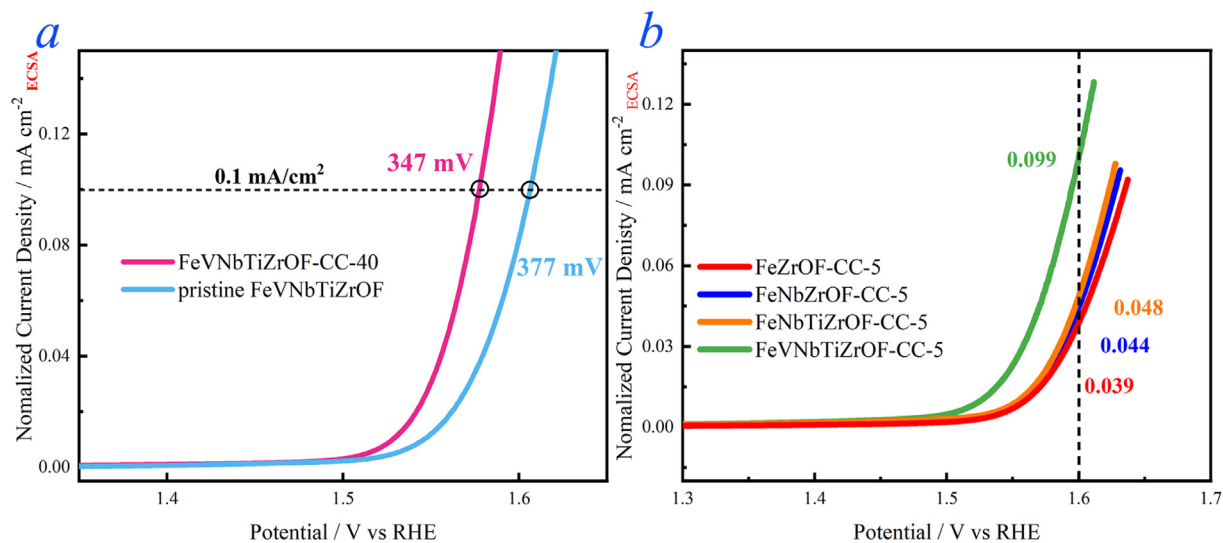
Fig. 7. The ECSA normalized polarization LSV curves of (a) the pristine and activated FeVNbTiZrOF; (b) FeZrOF-CC-5, FeNbZrOF-CC-5, FeNbTiZrOF-CC-5, and FeVNbTiZrOF-CC-5.

[47]. To corroborate this, we further compare the intrinsic activity of the activated oxyfluorides (Fig. 7b). As expected, continuously incorporation of more elements into single metal oxyfluoride greatly boosts its OER performance. For a selected applied potential of 1.6 V (vs RHE), FeVNbTiZrOF-CC-5 exhibits the highest normalized current density of 0.099 mA/cm^2 $_{ECSA}$, which is 2.06, 2.25, and 2.54 times higher than FeNbTiZrOF-CC-5, FeNbZrOF-CC-5, and FeZrOF-CC-5, respectively. Gradually adding inactive transition metal elements revises Fe species with optimal filling of e_g orbitals, among which V is the most efficient dopant. The outstanding

performance of the five-membered activated oxyfluoride confirms the synergistic effects of the within high-entropy configuration again. Integrating all the above-mentioned reasons makes the FeNbTiZrOF-CC-40 an active and stable water oxidation catalyst.

4. Conclusion

In summary, we in-situ activated and reconstructed the multi-metal oxyfluorides for advanced water oxidation through a chronopotentiometric method. The electrochemical reconstruction

modifies this compound with surface fluorine-leaching, formation of nanopores and most importantly the introduction of metal oxy-hydroxides. These extrinsic causes facilitate efficient electron/mass transfer at the electrode/electrolyte interface. Meanwhile, intrinsic proprieties including amorphous and high-entropy nature synergistically endow the five-membered oxyfluoride with higher density of coordinatively unsaturated sites and appropriate electronic structure, which would reduce the adsorption energy of intermediates as well as the energy barrier of OER, finally boosting the electrochemical catalytic performance. Hence, it only requires an overpotential of 348 ± 2 mV to reach the current density of 10 mA/cm^2 and a Tafel slope of 110.3 ± 0.1 mV/dec for catalytic kinetics, much better than the commercial RuO$_2$, the pristine counterpart and binary/ternary/quaternary activated metal oxyfluorides. This work provides new guidance for using electrochemical reconstruction to activate semiconductive oxyhalides and expanding their application for advanced water oxidation. Meanwhile, employment of inexpensive and inactive metal elements to establish high-entropy materials may point the next step of the research directions.

CRediT authorship contribution statement

Yin'an Zhu: Conceptualization, Formal analysis, Methodology. **Weiji Dai:** Software. **Xu Zhong:** Data curation. **Tao Lu:** Writing - review & editing. **Ye Pan:** Supervision, Writing - review & editing.

Declaration of Competing Interest

The authors declare that they have no known competing financial interests or personal relationships that could have appeared to influence the work reported in this paper.

Acknowledgements

Appendix A. Supplementary material

Supplementary data to this article can be found online at https://doi.org/10.1016/j.jcis.2021.05.170.

References

[1] T.R. Cook, D.K. Dogutan, S.Y. Reece, Y. Surendranath, T.S. Teets, D.G. Nocera, Solar energy supply and storage for the legacy and nonlegacy worlds, Chem. Rev. 110 (2010) 6474–6502, https://doi.org/10.1021/cr100246c.

[2] B.M. Hunter, H.B. Gray, A.M. Müller, Earth-Abundant Heterogeneous Water Oxidation Catalysts, Chem. Rev. 116 (2016) 14120–14136, https://doi.org/10.1021/acs.chemrev.6b00398.

[3] M. Povia, D.F. Abbott, J. Herranz, A. Heinritz, D. Lebedev, B.J. Kim, E. Fabbri, A. Patru, J. Kohlbrecher, R. Schäublin, M. Nachtegaal, C. Copéret, T.J. Schmidt, Operando X-ray characterization of high surface area iridium oxides to decouple their activity losses for the oxygen evolution reaction, Energy Environ. Sci. 12 (2019) 3038–3052, https://doi.org/10.1039/c9ee01018a.

[4] Q. Chen, Y. Fu, J. Jin, W. Zang, X. Liu, X. Zhang, W. Huang, Z. Kou, J. Wang, L. Zhou, L. Mai, In-situ surface self-reconstruction in ternary transition metal dichalcogenide nanorod arrays enables efficient electrocatalytic oxygen evolution, J. Energy Chem. 55 (2021) 10–16, https://doi.org/10.1016/j.jechem.2020.07.005.

[5] D. Chen, T. Liu, P. Wang, J. Zhao, C. Zhang, R. Cheng, W. Li, P. Ji, Z. Pu, S. Mu, Ionothermal route to phase-pure RuB2 catalysts for efficient oxygen evolution and water splitting in acidic media, ACS Energy Lett. 5 (2020) 2909–2915, https://doi.org/10.1021/acsenergylett.0c01384.

[6] P. Ji, X. Luo, D. Chen, H. Jin, Z. Pu, W. Zeng, J. He, H. Bai, Y. Liao, S. Mu, Significantly Improved Water Oxidation of CoP Catalysts by Electrochemical Activation, ACS Sustain. Chem. Eng. 8 (2020) 17851–17859, https://doi.org/10.1021/acssuschemeng.0c07169.

[7] D. Liu, H. Ai, J. Li, M. Fang, M. Chen, D. Liu, X. Du, P. Zhou, F. Li, K.H. Lo, Y. Tang, S. Chen, L. Wang, G. Xing, H. Pan, Surface Reconstruction and Phase Transition on Vanadium–Cobalt–Iron Trimetal Nitrides to Form Active Oxyhydroxide for Enhanced Electrocatalytic Water Oxidation, Adv. Energy Mater. 10 (2020) 1–9, https://doi.org/10.1002/aenm.202002464.

[8] Z. Kou, Y. Yu, X. Liu, X. Gao, L. Zheng, H. Zou, Y. Pang, Z. Wang, Z. Pan, J. He, S.J. Pennycook, J. Wang, Potential-Dependent Phase Transition and Mo-Enriched Surface Reconstruction of γ-CoOOH in a Heterostructured Co-Mo2C Precatalyst Enable Water Oxidation, ACS Catal. 10 (2020) 4411–4419, https://doi.org/10.1021/acscatal.0c00340.

[9] W. Dai, T. Lu, Y. Pan, Novel and promising electrocatalyst for oxygen evolution reaction based on MnFeCoNi high entropy alloy, J. Power Sources. 430 (2019) 104–111, https://doi.org/10.1016/j.jpowsour.2019.05.030.

[10] Y. Duan, S. Sun, Y. Sun, S. Xi, X. Chi, Q. Zhang, X. Ren, J. Wang, S.J.H. Ong, Y. Du, L. Gu, A. Grimaud, Z.J. Xu, Mastering Surface Reconstruction of Metastable Spinel Oxides for Better Water Oxidation, Adv. Mater. 31 (2019) 2–9, https://doi.org/10.1002/adma.201807898.

[11] W.H. Lee, J. Yi, H.N. Nong, P. Strasser, K.H. Chae, B.K. Min, Y.J. Hwang, H.S. Oh, Electroactivation-induced IrNi nanoparticles under different pH conditions for neutral water oxidation, Nanoscale 12 (2020) 14903–14910, https://doi.org/10.1039/d0nr02951c.

[12] J. Huang, Y. Li, Y. Zhang, G. Rao, C. Wu, Y. Hu, X. Wang, R. Lu, Y. Li, J. Xiong, Identification of Key Reversible Intermediates in Self-Reconstructed Nickel-Based Hybrid Electrocatalysts for Oxygen Evolution, Angew. Chemie - Int. Ed. 58 (2019) 17458–17464, https://doi.org/10.1002/anie.201910716.

[13] weiji Dai, X. Bai, Y. Zhu, Y. Zhang, T. Lu, Y. Pan, J. Wang, Surface reconstruction induced in-situ phosphorus doping in nickel oxides for enhanced oxygen evolution reaction, J. Mater. Chem. A. (2021) 6432–6441. https://doi.org/10.1039/d0ta10925h.

[14] Q. Wang, A. Sarkar, D. Wang, L. Velasco, R. Azmi, S.S. Bhattacharya, T. Bergfeldt, A. Düvel, P. Heitjans, T. Brezesinski, H. Hahn, B. Breitung, Multi-anionic and cationic compounds: New high entropy materials for advanced Li-ion batteries, Energy Environ. Sci. 12 (2019) 2433–2442, https://doi.org/10.1039/c9ee00368a.

[15] M. Kowalkińska, S. Dudziak, J. Karczewski, J. Ryl, G. Trykowski, A. Zielińska-Jurek, Facet effect of TiO2 nanostructures from TiOF2 and their photocatalytic activity, Chem. Eng. J. 404 (2021), https://doi.org/10.1016/j.cej.2020.126493.

[16] K. Liang, K. Marcus, Z. Yang, L. Zhou, H. Pan, Y. Bai, Y. Du, M.H. Engelhard, Y. Yang, Freestanding NiFe Oxyfluoride Holey Film with Ultrahigh Volumetric Capacitance for Flexible Asymmetric Supercapacitors, Small 14 (2018) 1–6, https://doi.org/10.1002/smll.201702295.

[17] M. Li, H. Liu, L. Feng, Fluoridation-induced high-performance catalysts for the oxygen evolution reaction: A mini review, Electrochem. Commun. 122 (2021), https://doi.org/10.1016/j.elecom.2020.106901 106901.

[18] K. Liang, L. Guo, K. Marcus, S. Zhang, Z. Yang, D.E. Perea, L. Zhou, Y. Du, Y. Yang, Overall Water Splitting with Room-Temperature Synthesized NiFe Oxyfluoride Nanoporous Films, ACS Catal. 7 (2017) 8406–8412, https://doi.org/10.1021/acscatal.7b02991.

[19] K. Lemoine, Z. Gohari-Bajestani, R. Moury, A. Terry, A. Guiet, J.M. Grenèche, A. Hémon-Ribaud, N. Heidary, V. Maisonneuve, N. Kornienko, J. Lhoste, Amorphous Iron-Manganese Oxyfluorides, Promising Catalysts for Oxygen Evolution Reaction under Acidic Media, ACS Appl. Energy Mater. 4 (2021) 1173–1181, https://doi.org/10.1021/acsaem.0c02417.

[20] K. Lemoine, J. Lhoste, A. Hémon-Ribaud, N. Heidary, V. Maisonneuve, A. Guiet, N. Kornienko, Investigation of mixed-metal (oxy)fluorides as a new class of water oxidation electrocatalysts, Chem. Sci. 10 (2019) 9209–9218, https://doi.org/10.1039/c9sc04027g.

[21] B. Zhang, K. Jiang, H. Wang, S. Hu, Fluoride-Induced Dynamic Surface Self-Reconstruction Produces Unexpectedly Efficient Oxygen-Evolution Catalyst, Nano Lett. 19 (2019) 530–537, https://doi.org/10.1021/acs.nanolett.8b04466.

[22] P. Chen, T. Zhou, S. Wang, N. Zhang, Y. Tong, H. Ju, W. Chu, C. Wu, Y. Xie, Dynamic Migration of Surface Fluorine Anions on Cobalt-Based Materials to Achieve Enhanced Oxygen Evolution Catalysis, Angew. Chem. Int. Ed. 57 (2018) 15471–15475, https://doi.org/10.1002/anie.201809220.

[23] D. Rodrigues, C. Cannes, N. Barré, D. Lambertin, S. Delpech, Role of fluoride ions on the uranium oxidation mechanism in highly alkaline solutions, Electrochim. Acta 266 (2018) 384–394, https://doi.org/10.1016/j.electacta.2018.02.046.

[24] M. Gong, H. Dai, A mini review of NiFe-based materials as highly active oxygen evolution reaction electrocatalysts, Nano Res. 8 (2015) 23–39, https://doi.org/10.1007/s12274-014-0591-z.

[25] W. Dononelli, G. Tomaschun, T. Klüner, L.V. Moskaleva, Understanding Oxygen Activation on Nanoporous Gold, ACS Catal. 9 (2019) 5204–5216, https://doi.org/10.1021/acscatal.9b00682.

[26] R. Li, X.J. Liu, H. Wang, D.Q. Zhou, Y. Wu, Z.P. Lu, Formation mechanism and characterization of nanoporous silver with tunable porosity and promising capacitive performance by chemical dealloying of glassy precursor, Acta Mater. 105 (2016) 367–377, https://doi.org/10.1016/j.actamat.2015.12.042.

[27] Y. Zhu, Y. Pan, E. Zhang, W. Dai, A self-assembled urchin-like TiO2@Ag-CuO with enhanced photocatalytic activity toward tetracycline hydrochloride degradation, New J. Chem. 44 (2020) 11076–11084. https://doi.org/10.1039/d0nj02153a.

[28] Y. Yang, H. Bao, H. Ni, X. Ou, S. Wang, B. Lin, P. Feng, Y. Ling, A novel facile strategy to suppress Sr segregation for high-entropy stabilized La0.8Sr0.2MnO3-δ cathode, J. Power Sources. 482 (2021) 228959. https://doi.org/10.1016/j.jpowsour.2020.228959.

[29] Y. Zhu, Y. Pan, W. Dai, T. Lu, Dealloying Generation of Oxygen Vacancies in the Amorphous Nanoporous Ni-Mo-O for Superior Electrocatalytic Hydrogen Generation, ACS Appl. Energy Mater. (2020), https://doi.org/10.1021/acsaem.9b01563.

[30] J. Jayaraj, D. Nanda Gopala Krishna, C. Mallika, U. Kamachi Mudali, Electrochemical Studies and XPS Analysis of the Surface of Zirconium-702 in Concentrated Nitric Acid With and Without Fluoride Ions, Trans. Indian Inst. Met. 71 (2018) 521–531. https://doi.org/10.1007/s12666-017-1165-z.

[31] J. Jayaraj, C. Thinaharan, S. Ningshen, C. Mallika, U. Kamachi Mudali, Corrosion behavior and surface film characterization of TaNbHfZrTi high entropy alloy in aggressive nitric acid medium, Intermetallics. 89 (2017) 123–132. https://doi.org/10.1016/j.intermet.2017.06.002.

[32] N. Duan, J. Yang, M. Gao, B. Zhang, J.L. Luo, Y. Du, M. Xu, L. Jia, B. Chi, J. Li, Multi-functionalities enabled fivefold applications of LaCo0.6Ni0.4O3−δ in intermediate temperature symmetrical solid oxide fuel/electrolysis cells, Nano Energy 77 (2020), https://doi.org/10.1016/j.nanoen.2020.105207 105207.

[33] I. Palacio, G. Otero-Irurueta, C. Alonso, J.I. Martínez, E. López-Elvira, I. Muñoz-Ochando, H.J. Salavagione, M.F. López, M. García-Hernández, J. Méndez, G.J. Ellis, J.A. Martín-Gago, Chemistry below graphene: Decoupling epitaxial graphene from metals by potential-controlled electrochemical oxidation, Carbon N. Y. 129 (2018) 837–846, https://doi.org/10.1016/j.carbon.2017.12.104.

[34] K. Wu, D. Shen, Q. Meng, J. Wang, Octahedral Co3O4 particles with high electrochemical surface area as electrocatalyst for water splitting, Electrochim. Acta 288 (2018) 82–90, https://doi.org/10.1016/j.electacta.2018.08.067.

[35] C. Pei, H. Chen, B. Dong, X. Yu, L. Feng, Electrochemical oxygen evolution reaction efficiently catalyzed by a novel porous iron-cobalt-fluoride nanocube easily derived from 3-dimensional Prussian blue analogue, J. Power Sour. 424 (2019) 131–137, https://doi.org/10.1016/j.jpowsour.2019.03.089.

[36] S. Xu, X. Gao, A. Deshmukh, J. Zhou, N. Chen, W. Peng, Y. Gong, Z. Yao, K.D. Finkelstein, B. Wan, F. Gao, M. Wang, M. Chen, H. Gou, Pressure-promoted irregular CoMoP2 nanoparticles activated by surface reconstruction for oxygen evolution reaction electrocatalysts, J. Mater. Chem. A 8 (2020) 2001–2007, https://doi.org/10.1039/c9ta11775j.

[37] M. Mathankumar, S. Anantharaj, A.K. Nandakumar, S. Kundu, B. Subramanian, Potentiostatic phase formation of β-CoOOH on pulsed laser deposited biphasic cobalt oxide thin film for enhanced oxygen evolution, J. Mater. Chem. A 5 (2017) 23053–23066, https://doi.org/10.1039/c7ta07410g.

[38] Y. Jin, M. Xie, S. Ai, J. Yang, Y. Yang, Y. Chen, In-Situ Generation of Oxide Nanowire Arrays from AgCuZn Alloy Sulfide with Enhanced Electrochemical Oxygen-Evolving Performance, ACS Appl. Mater. Interf. 7 (2015) 17112–17121, https://doi.org/10.1021/acsami.5b03805.

[39] Y. Liang, X. Sun, A.M. Asiri, Y. He, Amorphous Ni-B alloy nanoparticle film on Ni foam: Rapid alternately dipping deposition for efficient overall water splitting, Nanotechnology 27 (2016) https://doi.org/10.1088/0957-4484/27/12/12LT01.

[40] B.P. Mainali, D.K. Pattadar, F.P. Zamborini, Size-Dependent Ripening of Gold Nanoparticles through Repetitive Electrochemical Surface Oxidation-Reduction Cycling, J. Electrochem. Soc 167 (2020), https://doi.org/10.1149/1945-7111/abbd72 146503.

[41] S. Sun, H. Li, Z.J. Xu, Impact of Surface Area in Evaluation of Catalyst Activity, Joule 2 (2018) 1024–1027, https://doi.org/10.1016/j.joule.2018.05.003.

[42] T.X. Nguyen, Y.H. Su, C.C. Lin, J. Ruan, J.M. Ting, A New High Entropy Glycerate for High Performance Oxygen Evolution Reaction, Adv. Sci. 2002446 (2021) 1–11, https://doi.org/10.1002/advs.202002446.

[43] H. Han, H. Choi, S. Mhin, Y.R. Hong, K.M. Kim, J. Kwon, G. Ali, K.Y. Chung, M. Je, H.N. Umh, D.H. Lim, K. Davey, S.Z. Qiao, U. Paik, T. Song, Advantageous crystalline-amorphous phase boundary for enhanced electrochemical water oxidation, Energy Environ. Sci. 12 (2019) 2443–2454, https://doi.org/10.1039/c9ee00950g.

[44] G. Chen, Y. Zhu, H.M. Chen, Z. Hu, S.F. Hung, N. Ma, J. Dai, H.J. Lin, C. Te Chen, W. Zhou, Z. Shao, An Amorphous Nickel–Iron-Based Electrocatalyst with Unusual Local Structures for Ultrafast Oxygen Evolution Reaction, Adv. Mater. 31 (2019) 1–7, https://doi.org/10.1002/adma.201900883.

[45] Y. Liu, Q. Li, R. Si, G.D. Li, W. Li, D.P. Liu, D. Wang, L. Sun, Y. Zhang, X. Zou, Coupling Sub-Nanometric Copper Clusters with Quasi-Amorphous Cobalt Sulfide Yields Efficient and Robust Electrocatalysts for Water Splitting Reaction, Adv. Mater. 29 (2017), https://doi.org/10.1002/adma.201606200.

[46] T. Löffler, H. Meyer, A. Savan, P. Wilde, A. Garzón Manjón, Y.T. Chen, E. Ventosa, C. Scheu, A. Ludwig, W. Schuhmann, Discovery of a Multinary Noble Metal-Free Oxygen Reduction Catalyst, Adv. Energy Mater. 8 (2018) 1–7, https://doi.org/10.1002/aenm.201802269.

[47] M. Cui, C. Yang, B. Li, Q. Dong, M. Wu, S. Hwang, H. Xie, X. Wang, G. Wang, L. Hu, High-Entropy Metal Sulfide Nanoparticles Promise High-Performance Oxygen Evolution Reaction, Adv. Energy Mater. 11 (2021) 1–8, https://doi.org/10.1002/aenm.202002887.

[48] R.Q. Yao, Y.T. Zhou, H. Shi, W. Bin Wan, Q.H. Zhang, L. Gu, Y.F. Zhu, Z. Wen, X.Y. Lang, Q. Jiang, Nanoporous Surface High-Entropy Alloys as Highly Efficient Multisite Electrocatalysts for Nonacidic Hydrogen Evolution Reaction, Adv. Funct. Mater. 2009613 (2020) 1–9. https://doi.org/10.1002/adfm.202009613.

[49] D. Zhang, Y. Shi, H. Zhao, W. Qi, X. Chen, T. Zhan, S. Li, B. Yang, M. Sun, J. Lai, B. Huang, L. Wang, The facile oil-phase synthesis of a multi-site synergistic high-entropy alloy to promote the alkaline hydrogen evolution reaction, J. Mater. Chem. A. 9 (2021) 889–893, https://doi.org/10.1039/d0ta10574k.

[50] T.A.A. Batchelor, J.K. Pedersen, S.H. Winther, I.E. Castelli, K.W. Jacobsen, J. Rossmeisl, High-Entropy Alloys as a Discovery Platform for Electrocatalysis, Joule 3 (2019) 834–845, https://doi.org/10.1016/j.joule.2018.12.015.

[51] Z. Jin, J. Lv, H. Jia, W. Liu, H. Li, Z. Chen, X. Lin, G. Xie, X. Liu, S. Sun, H.J. Qiu, Nanoporous Al-Ni-Co-Ir-Mo High-Entropy Alloy for Record-High Water Splitting Activity in Acidic Environments, Small 15 (2019) 1–7, https://doi.org/10.1002/smll.201904180.

[52] H. Li, Y. Han, H. Zhao, W. Qi, D. Zhang, Y. Yu, W. Cai, S. Li, J. Lai, B. Huang, L. Wang, Fast site-to-site electron transfer of high-entropy alloy nanocatalyst driving redox electrocatalysis, Nat. Commun. 11 (2020) 1–9, https://doi.org/10.1038/s41467-020-19277-9.